Band shaping and emission control via waveguide plasmon polaritons

Augusto Martins,[1] Aimi Abass,[2] Ben-Hur V. Borges,[1] and Emiliano R. Martins[1,*]
[1]*Department of Electrical and Computer Engineering, University of São Paulo, CEP 13566-590, São Carlos, SP, Brazil*
[2]*Herzogstrasse 12, 52070, Aachen, Germany*

(Received 18 March 2021; revised 26 April 2021; accepted 28 April 2021; published 19 May 2021)

Photonic nanostructures can improve the efficiency and functionality of optoelectronic devices by controlling propagation and extraction of light in waveguides. The paradigmatic example is the extraction of light by matching the grating and waveguide mode momenta. A higher functionality can be achieved, however, via strong coupling between waveguide and plasmon modes. Here, we show that such hybridized systems provide a convenient strategy to tailor the dispersion band of the waveguide. By controlling the metallic grating height, the bands evolve from a Dirac cone to a flatband and a parabolic profile. We show an application of this system to light emitting waveguides, where a flatband leads to a sharply defined emission cone, with a 1.8 fold gain in emission efficiency and a Purcell factor of 2.4. We show that 72.2% of all radiated power is contained within the flatband region and is eight times larger than the total emission by the dipole in a homogenous medium. The system thus combines efficiency gain with the opportunity of beam shaping.

DOI: 10.1103/PhysRevB.103.205423

I. INTRODUCTION

Though light propagation can be controlled with various macro-optical components involving mirrors and lenses, such solutions are often costly and come with large spatial requirements, as they rely on geometrical optics. Both spatial requirements and costs can easily exceed by orders of magnitude what is required for the emitter. As a result, compact alternative photonic solutions provided by nanostructures have gained widespread interest over the last two decades. In particular, these structures can be used to control the spontaneous emission of quantum dots (QDs) or dye molecules [1–5] by altering their local photonic density of states (PDOS) [6–8]. The emission rate and angular pattern can be readily tailored by engineering the nanostructures with a judicious choice of materials and geometry [9,10].

One promising approach is to use photonic cavities, which offer the opportunity to simultaneously control the photonic density of states and angular emission [11,12]. A common approach is to embed the emitters in waveguides, thereby confining light in at least one dimension, and then employ nanostructures to extract light trapped by total internal reflection [11,13]. The nanostructures can also act as the cavity itself, and multiple cavities (or resonators) can be associated to form a metasurface [3]. These approaches have led to emitters with directional radiation patterns [14–16] or with engineered profiles [7,17–20] without the need of external optical components or complex surface shaping.

Here, we explore the physics in sculpting the dispersion of hybridized photonic-plasmonic systems and demonstrate the ability to realize various dispersion shapes, from a Dirac cone to a flatband and a parabolic band. We demonstrate interesting radiation distribution achieved by this route, such as a homogeneous light intensity distribution within a sharply defined angular window. The ease in controlling the coupling of photonic and plasmonic modes adds an important degree of freedom to the control of light emission and band shaping, with applications in light emitting devices (LEDs), sensors, camera flashes, automotive lighting, slow light, and to the growing field of photonic flatbands [21]. In Sec. II, we focus our attention on how hybridized photonic-plasmonic modes (i.e., a supermode that arises from strong coupling between these two modes) can lead to band shaping and, in particular, to the emergence of flat dispersion bands. In Sec. III, we show that the same effect can be achieved in a simplified system. In Sec. IV, we explore a flat dispersion band to taylor the light emitting properties of waveguides, achieving emission in a well defined angular cone. The paper is concluded in Sec. V.

II. DISPERSION MANAGEMENT IN A HYBRID PLASMONIC WAVEGUIDE SYSTEM

We begin the analysis by considering the hybridization between a waveguide mode with a plasmonic mode forming a waveguide plasmon polariton (WPP) [22]. Recently, it has been shown that such coupled systems can support bound states in the continuum (BICs), which are exotic modes with infinite lifetime in spite of being coupled to radiative channels [23]. One important advantage of waveguide plasmon polariton modes is the opportunity of combining the strong light interaction of plasmonic modes with the low material losses of photonic waveguide modes.

To identify the mechanisms behind the modes coupling, we first consider a slab waveguide (300 nm thick) embedded in an $n = 1.45$ medium as shown in Fig. 1 with a double grating system. Though seemingly complex, this double grating waveguide system is a suitable model that provides clarity

*erm@usp.br

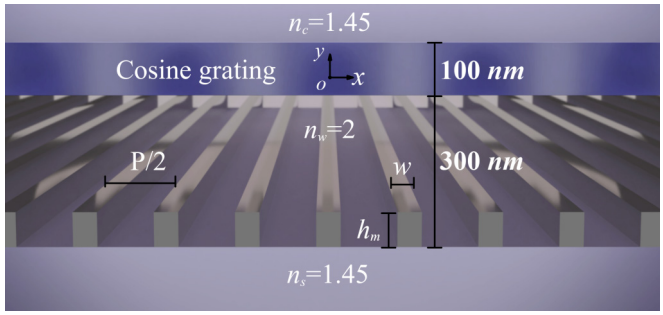

FIG. 1. Double grating assisted waveguide system representation. The system is composed of a 300 nm thick waveguide (refractive index $n_w = 2$) embedded in an $n = 1.45$ medium. Above the waveguide there is a 100 nm thick cosine grating with period $P =$ 360 nm. This grating is defined by $\epsilon(x) = 1.45^2 + 1.45\cos(Gx)$, where $G = 2\pi/P$ is the grating momentum. Finally, inside the waveguide there is an Ag grating with period $P/2$, width $w = 60$ nm, and height h_m. Notice that the ridges are aligned with the peaks and valleys of the cosine grating.

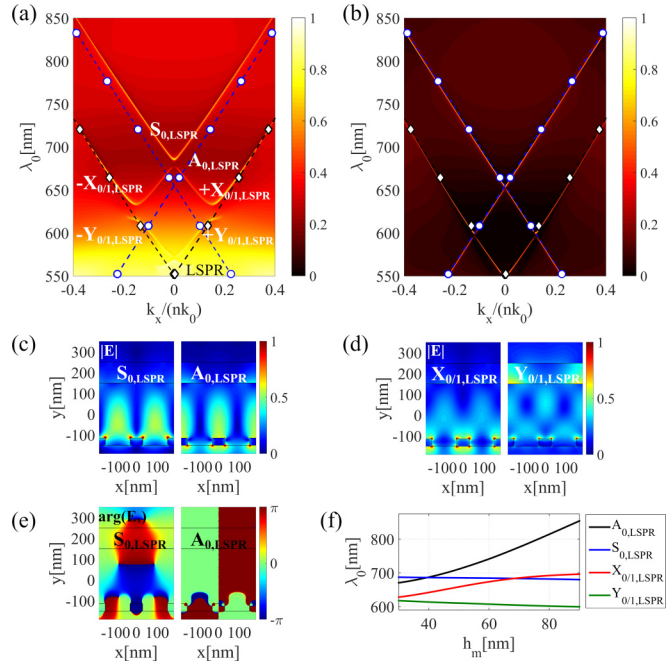

FIG. 2. (a) Extinction dispersion (colorbar shows the magnitude) for TM excitation (magnetic field along z, H_z, in Fig. 1) of the double grating assisted waveguide system with $h_m = 35$ nm. The dashed lines with blue circles (black diamonds) mark the TM_0 (TM_1) bare waveguide mode dispersion, folded into the first Brillouin zone. (b) System extinction dispersion (colorbar magnitude) without the metallic grating. (c) Electric field amplitude distribution for the $S_{0,LSPR}$ ($\lambda_0 = 686.5$ nm, left) and $A_{0,LSPR}$ ($\lambda_0 = 678$ nm, right) modes at the Γ point [$k_x = 0$ in (a)] for $h_m = 35$ nm. (e) Phase (argument) distribution of the x component of the electric field for the $S_{0,LSPR}$ ($\lambda_0 = 686.5$ nm, left) and $A_{0,LSPR}$ ($\lambda_0 =$ 678 nm, right) modes at the Γ point [$k_x = 0$ in (a)] for $h_m = 35$ nm. Note that the $A_{0,LSPR}$ and $S_{0,LSPR}$ field distributions are asymmetric and symmetric, respectively. (d) Electric field amplitude distributions for the $\pm X_{0/1,LSPR}$ ($\lambda_0 = 634$ nm, left) and $\pm Y_{0/1,LSPR}$ ($\lambda_0 =$ 615 nm, right) modes at $k_x = \pm 0.16nk_0$. (f) shows the eigenvalue as a function of the metallic grating height for the $A_{0,LSPR}$ (black line) and $S_{0,LSPR}$ (blue line) modes at the Γ point and the $\pm X_{0/1,LSPR}$ (red line) and $\pm Y_{0/1,LSPR}$ (green line) modes $k_x = \pm 0.16nk_0$.

in analyzing the underlying hybridization and band shaping physics as it makes it easier to identify the role played by each grating component. To be more specific, the top 1D dielectric grating (period $P = 360$ nm) provides diffractive coupling between waveguided and radiation modes, while the 1D metal nanoantenna array (period $P/2$) main role is to provide the localized surface plasmon resonance (LSPR) mode in the system. Note that, due to its half-period, the metallic grating only couples counterpropagating guided modes, but not guided to radiated modes. By not burdening the metallic grating with a diffraction functionality, this system provides clarity in the role of each grating and each mode as the LSPR will be largely unchanged by the top dielectric grating.

The top grating has permittivity distribution $\epsilon(x) = 1.45^2 + 1.45\cos(Gx)$, where $G = 2\pi/P$. The period was chosen to couple the incident light, whose wavelengths are around 700 nm, with the two lowest order transversal magnetic (TM) modes of the waveguide. The bottom grating is made of Ag ridges with thickness h_m and width $w = 60$ nm, which was chosen to guarantee that the ridges support LSPR at wavelengths shorter than 600 nm for $h_m \in$ [20 nm, 120 nm]. Additionally, the ridges are aligned with the cosine grating peaks and valleys, thus making the system mirror symmetric with respect to the $x = 0$ plane. The coupling strength is aided by the excitation of LSPRs in the structure, leading to the formation of strong field enhancement [23,24].

The system extinction dispersion (defined as $1 - T$, where T is the system zeroth-order transmittance under plane wave excitation) for TM polarization (magnetic field along z, H_z, in Fig. 1) is calculated using the rigorous coupled wave analysis (RCWA) [9,25,26]. Figure 2(a) shows the extinction for 35 nm tall ridges. The dashed lines with blue circles (black diamonds) mark the TM_0 (TM_1) mode dispersion of the bare waveguide (without the gratings), folded into the first Brillouin zone. Five resonance bands can be distinguished in Fig. 2(a); they are four WPP modes ($A_{0,LSPR}$, $S_{0,LSPR}$, $X_{0/1,LSPR}$, and $Y_{0/1,LSPR}$) and a low-Q LSPR at around 550 nm. The subscripts refer to the uncoupled waveguide and LSPR modes that compose the WPP modes. The WPP resonances result from the coupling between counterpropagating waveguide modes and the LSPR [23,24]. The presence of band gaps and avoided crossings in the resonances are characteristics of the coupling between those modes [27,28]. The band gap at the Γ point ($k_x = 0$) at around $\lambda_0 = 670$ nm results from the coupling between counterpropagating TM_0 modes and the LSPR mode. Thus, we label the resulting WPP modes as $A_{0,LSPR}$ and $S_{0,LSPR}$ modes. The labels A and S refer to the symmetry of the modes, as detailed below [Figs. 2(c) and 2(e)]. The next band gaps occur at $k_x = \pm 0.16nk_0$ and are due to the coupling between the counterpropagating $\pm TM_0$ and $\mp TM_1$ modes (the sign refers to the direction of propagation of the bare waveguide modes), enhanced by the LSPR. Due to the coupling between these two different waveguide modes, these WPP modes are labeled $\pm X_{0/1,LSPR}$ and $\pm Y_{0/1,LSPR}$ (the signs refer to the k-space

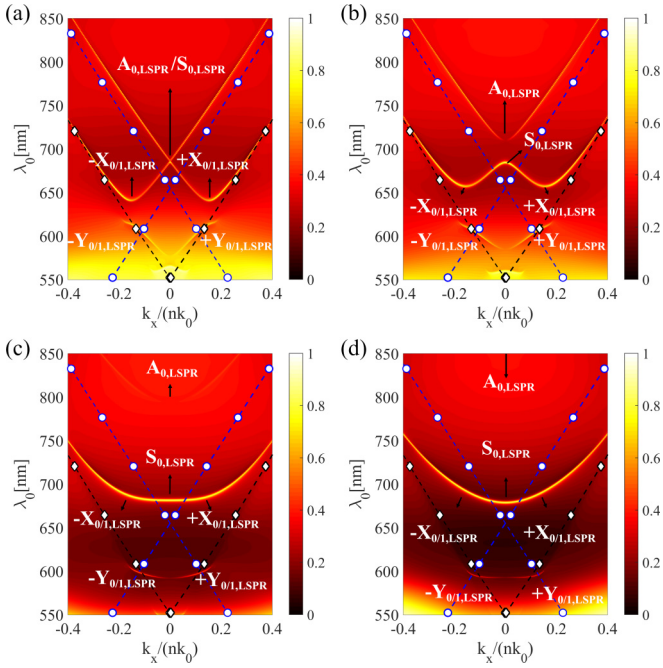

FIG. 3. (a)–(d) Show the extinction dispersion at TM excitation (magnetic field along z, H_z, in Fig. 1) of the double grating assisted waveguide system for Ag grating height of 39.5 nm, 50 nm, 75 nm, and 90 nm, respectively. The dashed lines with blue circles (black diamonds) mark the TM_0 (TM_1) bare waveguide mode dispersion, folded into the first Brillouin zone.

position in the dispersion). The role played by the LSPR mode can be qualitatively assessed by comparing the system extinction with [Fig. 2(a)] and without the metallic grating [Fig. 2(b)]. In the former, the LSPR mode both strengthens the coupling between counterpropagating waveguide modes and also hybridizes along with these modes, resulting in a strong band distortion. In contrast, in the latter the coupling is dominated only by the second-order Bragg reflection [28], which is much weaker, thus resulting in a modest band-gap opening and a negligible band distortion, as shown in Fig. 2(b). Such an LSPR enhanced coupling allows a convenient mechanism for band shaping, as detailed in Fig. 3.

Next, we show how the dispersion can be tuned by adjusting the coupling strength. To describe the band shaping, we focus attention on the WPP modes, whose electric fields are shown in Figs. 2(c) and 2(d). Figure 2(c) left shows the mode profile of the $S_{0,LSPR}$ mode, which is symmetric [see the phase distribution shown in Fig. 2(e) left] and lies at the Γ point of the upper band (larger wavelength), at $\lambda_0 = 686.5$ nm [see Fig. 2(a)]. Figure 2(c) right shows the mode profile of the $A_{0,LSPR}$, which is asymmetric [see the phase distribution shown in Fig. 2(e) right] and lies at the Γ point of the lower band at $\lambda_0 = 678$ nm. The asymmetric field profile of this mode prevents it from coupling with a plane wave at normal incidence, which is characteristic of a symmetry protected BIC. Finally, the $\pm X_{0/1,LSPR}$ and $\pm Y_{0/1,LSPR}$ modes, whose field distributions are shown in Fig. 2(d) left and right, respectively, lie at $k_x = \pm 0.16nk_0$. Note that the electric field is strongly concentrated above the metallic ridges for the modes $A_{0,LSPR}$ [Fig. 2(c) right] and $\pm X_{0/1,LSPR}$ [Fig. 2(d) left]. It is expected, therefore, that these modes will be more strongly affected by the tuning of the LSPR mode through the metallic grating geometry. Indeed, as shown in Fig. 2(f), these modes resonant wavelengths are the most sensitive to variations in the metallic ridge thickness. In contrast, the electric field distributions of the $S_{0,LSPR}$ and $\pm Y_{0/1,LSPR}$ modes have a minimum above the metallic ridges, as shown in Figs. 2(c) left and 2(d) right, respectively. Therefore, they are less sensitive to the tuning of the LSPR, as shown in the blue and green curves in Fig. 2(f). Interestingly, the $S_{0,LSPR}$ eigenvalue curve is crossed by the $A_{0,LSPR}$ and $\pm X_{0/1,LSPR}$ modes at $h_m = 39.5$ nm and $h_m = 70$ nm, respectively, as shown in Fig. 2(f). These crossings have great influence on the band shaping, as will be shown next. The first crossing occurs at the threshold of a band flipping [28], upon which the modes $A_{0,LSPR}$ and $S_{0,LSPR}$ switch their bands in the extinction dispersion. Lastly, the proximity between the three modes ($\pm X_{0/1,LSPR}$ and $S_{0,LSPR}$) in the second crossing leads to the formation of a flatband.

To better understand the relationship between the mode crossings and the flatband formation, the dispersion bands for four different coupling conditions are shown in Fig. 3. With $h_m = 39.5$ nm, the Γ point modes ($A_{0,LSPR}$ and $S_{0,LSPR}$) are degenerated, leading to the formation of a Dirac point, as shown in Fig. 3(a). Interestingly, as shown in Fig. 2(f), for h_m beyond the crossing point, the modes swap their position in the spectrum, causing a band flip: Now, the (leaky) $S_{0,LSPR}$ mode lies in the lower band while the $A_{0,LSPR}$, which is a symmetry protected BIC, lies in the top band, as their resonances in Fig. 3(b) for $h_m = 50$ nm indicate. The band flipping is closely related to the interplay between the Fourier harmonics of the Bragg resonances [28]. Note that, for $h_m > 39.5$ nm, the $S_{0,LSPR}$ and $\pm X_{0/1,LSPR}$ modes lie at the same band, resulting in a w-shaped dispersion when $h_m = 50$ nm. The wavelengths of these modes, as shown in Fig. 2(f), can be brought closer together by increasing the metallic ridge height, thus strengthening the LSPR and mode coupling. Such a feature leads to the formation of a flatband, as shown in Fig. 3(c), for $h_m = 75$ nm. Beyond this point, the further redshifting of the $\pm X_{0/1,LSPR}$ modes leads to a parabolic dispersion shape, as shown in Fig. 3(d). Therefore, by controlling the LSPR mode enhanced coupling, the dispersion of the WPP modes can be conveniently engineered, from a Dirac point, to a w-shaped dispersion, flatband, and finally to a parabolic shape.

III. SIMPLIFIED SYSTEM

In the previous section, we employed a double-grating system to distinguish between coupling from free space radiation to guided modes (provided by the dielectric grating) and LSPR enhanced coupling between different guided modes. We concluded that the mode dispersion shaping was due to an interplay between the increased coupling among the TM_0 and TM_1 Bragg resonances and the LSPR mode. Having ascertained the underlying physics, we show here that a similar effect can be obtained with a single metallic grating with larger period, designed to perform both tasks simultaneously. The metallic grating of the simplified system would of course need to be adjusted, as shown in Fig. 4(a). Thus, the waveguide thickness is reduced to 190 nm (to blueshift the flatband and position it in the visible range) and the metallic grating

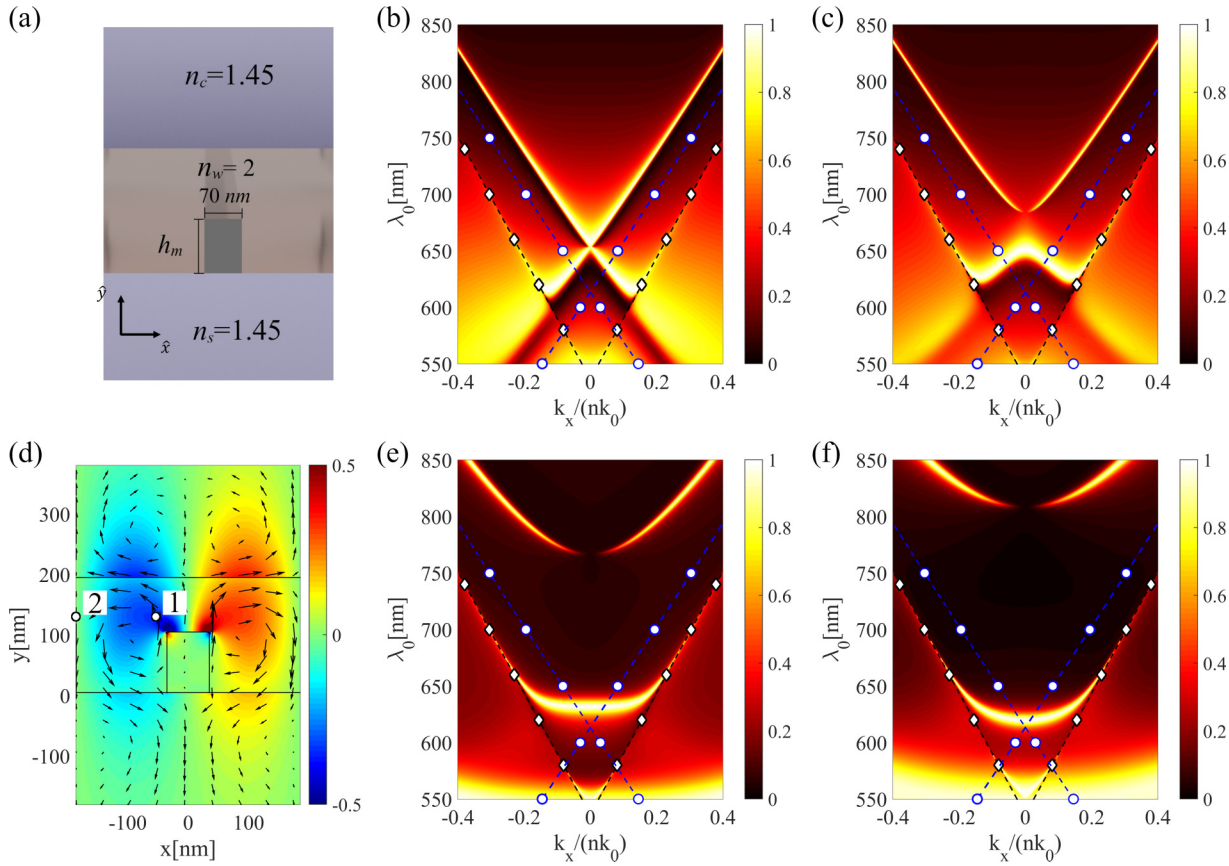

FIG. 4. (a) Simplified system representation. The system is composed of a 190 nm thick waveguide (refractive index $n_w = 2$) embedded in an $n = 1.45$ medium. In the waveguide there is an Ag grating with period $P = 370$ nm, width $w = 70$ nm, and height h_m. (b), (c), (e), and (f) extinction dispersion of the simplified system with h_m equal to 40 nm, 60 nm, 100 nm, and 120 nm, respectively. The dashed lines with blue circles mark the TM_0 bare waveguide mode dispersion, folded into the first Brillouin zone. The dashed lines with black diamonds mark the Rayleigh anomalies ($m = \pm 1$) to the substrate. (d) Shows the $\hat{y}$ component of the electric field at the flatband ($h_m = 100$ nm and $\lambda_0 = 634$ nm) at normal incidence. The vector field represents the average Poynting vector of this mode. The coordinates of points 1 and 2 are (−75 nm, 145 nm) and (−185 nm, 145 nm), respectively.

period P is increased to 370 nm after a fine tuning of the flatband. Figures 4(b), 4(c), 4(e), and 4(f) show the dispersion extinction for Ag grating heights (h_m) of 40 nm, 60 nm, 100 nm, and 120 nm, respectively. As in the previous system, the band resonances also suffer strong reshaping as the metallic grating height is increased. The band reshaping again ranges from a Dirac point [Fig. 4(b)], to a w-shaped band [Fig. 4(c)], a flatband [Fig. 4(e)], and a parabola [Fig. 4(f)]. Note that, in this system, the TM_1 mode is cut off, and the LSPR mode couples the TM_0 with the Rayleigh anomaly to the substrate. Band reshaping, therefore, does not require multimode operation.

IV. DIPOLE EMISSION IN THE FLATBAND CONDITION

As an application example of band shaping, we demonstrate emission control through exploiting a structure which supports a flatband, resulting from a hybrid plasmonic photonic mode. We consider the emission of a dipole line source placed inside the waveguide structure, as indicated in Fig. 4(d). The grating ridge thickness is $h_m = 100$ nm, resulting in the flatband shown in Fig. 4(e). The emission angular dependence is also calculated using the RCWA [9,25,26,29]. First, we place a $\hat{y}$-oriented dipole at point 1 [see Fig. 4(d)]. The resulting normalized emission dispersion (radiated power density spectrum) to the substrate and cover are shown in Figs. 5(a) and 5(b), respectively. Note that they closely resemble the plane-wave extinction shown in Fig. 4(e) featuring a flatband around 634 nm. Nevertheless, when the dipole is displaced to point 2 [see Fig. 4(d)], it cannot couple with the flatband mode, as shown by the emission dispersions towards the substrate and cover in Figs. 5(c) and 5(d), respectively. This is due to the phase symmetry mismatch between the dipole radiated field distribution and the mode pattern. Indeed, the $\hat{y}$ component of the electric field radiation of a $\hat{y}$-oriented dipole has a symmetric distribution. However, the mode field distribution is predominantly even for a transverse plane cutting point 1 but predominantly odd around point 2; consequently, coupling for a dipole at point 2 is symmetry forbidden.

To assess how the emission depends on the dipole location, we evaluate it at the flatband wavelength ($\lambda_0 = 634$ nm) as a function of x with the vertical position fixed at $y = 145$ nm. The resulting normalized emission dispersion to the cover and substrate are shown in Figs. 6(a) and 6(b), respectively, for a $\hat{y}$-oriented dipole. The results for an x-oriented dipole

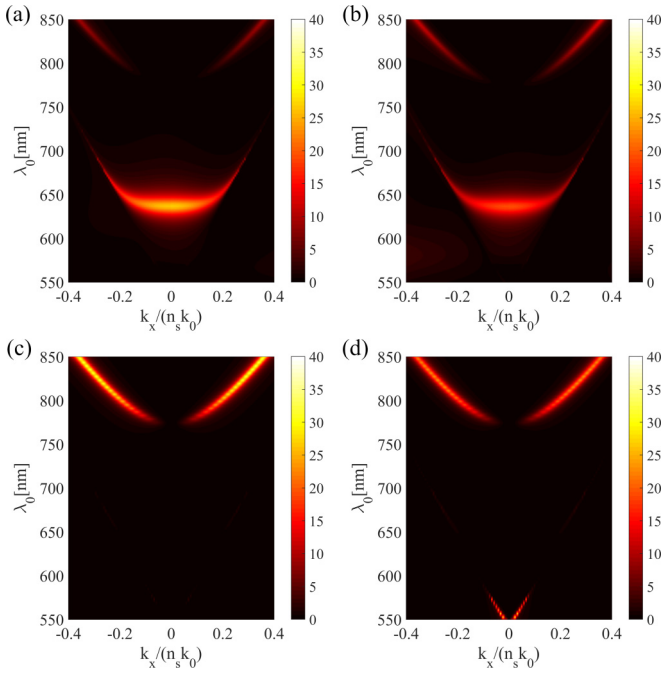

FIG. 5. (a) and (b) [(c) and (d)] show the normalized emission dispersion of a $\hat{y}$-oriented dipole in the simplified system with $h_m =$ 100 nm at point 1 (−75 nm, 145 nm) [2 (−185 nm, 145 nm)] to the substrate and cover, respectively. Points 1 and 2 are marked in Fig. 4(d). The plots are normalized to the perpendicular emission of randomly oriented dipoles in the absence of the metallic grating.

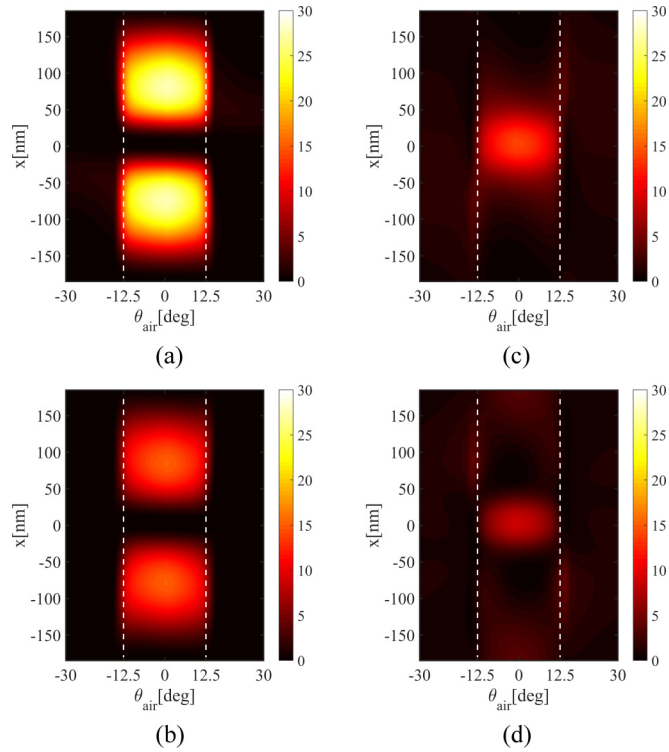

FIG. 6. (a) and (b) [(c) and (d)] show the normalized emission towards the cover and substrate, respectively, of a $\hat{y}$- [x-]oriented dipole as a function of its x coordinate, at $y = 145$ nm. The operating wavelength is 634 nm. The dashed lines mark the emission cone of the dipoles. Notice that the angles are defined with respect to propagation in air. The plots are normalized to the perpendicular emission of randomly oriented dipoles in the absence of the metallic grating.

are shown in Figs. 6(c) and 6(d). The emission of the $\hat{y}$-oriented dipole shows two regions of field maximum where the coupling strength is high due to symmetry compatibility. The x-oriented dipole, in contrast, has one strong lobe around $x = 0$ [see Figs. 6(c) and 6(d)] due to the dipole asymmetric (symmetric) $\hat{y}$- (x)-oriented electric field distribution, which is the opposite of a $\hat{y}$-oriented dipole. Additionally, the x-oriented dipole cannot couple efficiently around ±185 nm. Indeed, it mostly radiates to the cover and substrate without interacting substantially with the system because it is too far away from the Ag ridges. The emission maps, therefore, indicate that a random distribution of emitters in the system results in a uniform emission confined to a well-defined angular cone (25 degrees in air).

To further characterize the light-matter interaction in the system, we calculate the angular-dependent radiation for vertical [Fig. 7(a)] and horizontal [Fig. 7(b)] dipole emissions. The plots are normalized to the perpendicular emission of randomly oriented dipoles in the absence of the metallic grating. Figure 7(c) shows the average between horizontal and vertical emissions. Figures 7(a)–7(c) also show the emission of the dipoles without the metallic grating (dashed lines). The inclusion of the grating mostly increases the radiation in the flatband region without significantly perturbing the remaining parts of the radiation pattern (compare the solid lines with the dashed lines in Fig. 7). This increase amounts to a 9.19-fold and a 8.39-fold gain in the power emitted within the flatband region (25 degrees cone) towards the substrate and cover, respectively. The ability to obtain such a homogeneous power distribution with flexible control over the angular span is of great importance for LEDs and its various applications for two main reasons. First, it potentially allows efficient light extraction from LED systems because only a limited angular range from the emitter needs to be considered. Second, a plateau shaped radiant intensity distribution would be desirable for various applications that require a homogeneous light intensity distribution within a specific angular window, such as sensors, camera flashes, and automotive lighting. Achieving this plateaued angular distribution with our proposed structure also sidesteps the need to resort to additional external macro-optical components, therefore enabling a compact implementation fitted for device miniaturization.

Finally, we calculate the Purcell factor, which is defined as the ratio between the total power emitted by the dipole when located in the corrugated waveguide, to the power emitted when the dipole is located in a homogeneous medium with refractive index $n = 2$. The normalized radiated power has a similar definition, but it only considers radiated power (as opposed to absorbed). The calculation of the emitted power assumes a random spatial distribution of dipoles and random orientation. The resulting Purcell factor is 2.43. It is important to notice that the Purcell factor includes absorption in the metallic grating. If only radiated power is considered (instead of emitted power), we find a 1.8 fold increase in radiated power, out of which 72.2% is emitted within the flatband

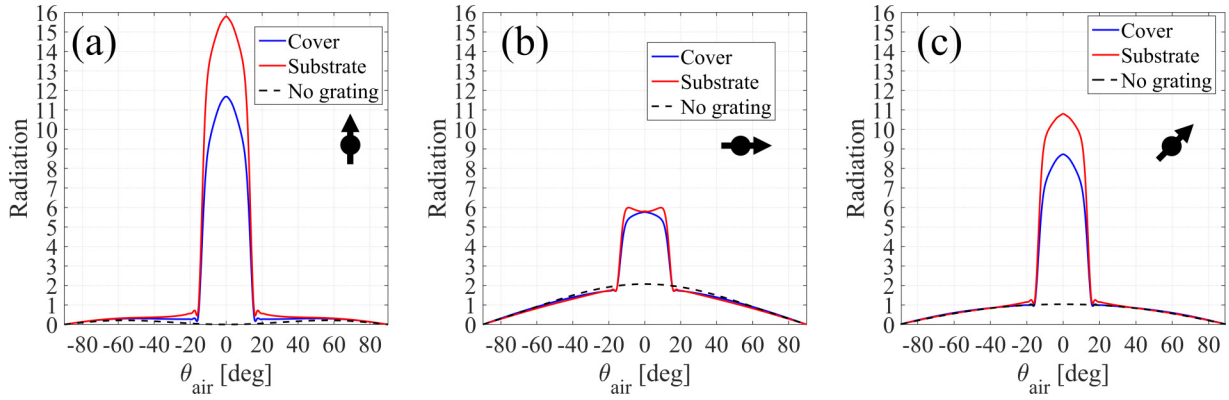

FIG. 7. Averaged and normalized radiation pattern to the cover (blue), substrate (red), and without the metallic grating (cover and substrate, dashed black) of homogeneously distributed $\hat{y}$-oriented (a) and x-oriented (b) dipoles inside the unit cell. The operating wavelength is 634 nm. (c) Shows the average of (a) and (b) (solid lines) and the emission without the metallic grating (dashed). The average emission without the metallic grating is the same towards the cover and substrate. All curves were normalized with respect to the average perpendicular emission of randomly oriented dipoles in the system without the waveguide.

region. Therefore, it is clear that the radiation gain due to an enhancement of the local density of states provided by the metallic grating compensate for its absorption losses.

V. CONCLUSION

In conclusion, we have shown that a photonic structure supporting hybridized photonic-plasmonic modes allows straightforward band shaping with large flexibility by tuning the coupling strength between these modes. At the weak coupling regime, the band profile features a Dirac cone, and evolves continuously to w-shape, flatband, and parabolic shape as the coupling is increased. We exploited the band shaping possibilities to control the angular radiation pattern of emitters embedded in the nanopatterned waveguide. In particular, we demonstrated a system which supports a WPP with an extremely wide flatband dispersion such that the emitters embedded within the system dominantly emit within the defined angular span of 25 degrees, creating a homogeneous power distribution in that angular range. Such homogeneous radiant intensity distribution would be desirable for various applications that require homogeneous light intensity distribution within a specific angular window, such as sensors, camera flashes, and automotive lighting. Achieving this plateaued angular distribution with our proposed structure also sidesteps the need to resort to additional external macro-optical components, enabling a compact implementation fitted for device miniaturization. We finally note that the same effect can also be achieved in a 3D system by considering 2D metallic nanoantenna arrays inside a waveguide slab.

ACKNOWLEDGMENTS

This work is supported by São Paulo Research Foundation (FAPESP) (Grants No. 2013/07276-1, No. 2015/21455-1, and No. 2020/00619-4).

[1] G. Lozano, S. R. Rodriguez, M. A. Verschuuren, and J. G. Rivas, Metallic nanostructures for efficient LED lighting, Light: Science & Applications **5**, e16080 (2016).

[2] S. Wu, H. Xia, J. Xu, X. Sun, and X. Liu, Manipulating luminescence of light emitters by photonic crystals, Adv. Mater. **30**, 1803362 (2018).

[3] A. Vaskin, R. Kolkowski, A. F. Koenderink, and I. Staude, Light-emitting metasurfaces, Nanophotonics **8**, 1151 (2019).

[4] H. S. Wasisto, J. D. Prades, J. Gülink, and A. Waag, Beyond solid-state lighting: Miniaturization, hybrid integration, and applications of gan nano- and micro-leds, Appl. Phys. Rev. **6**, 041315 (2019).

[5] I. Staude, T. Pertsch, and Y. S. Kivshar, All-dielectric resonant meta-optics lightens up, Acs Photonics **6**, 802 (2019).

[6] V. Giannini, A. I. Fernández-Domínguez, S. C. Heck, and S. A. Maier, Plasmonic nanoantennas: Fundamentals and their use in controlling the radiative properties of nanoemitters, Chem. Rev. **111**, 3888 (2011).

[7] S. Liu, A. Vaskin, S. Addamane, B. Leung, M.-C. Tsai, Y. Yang, P. P. Vabishchevich, G. A. Keeler, G. Wang, and X. He, Light-emitting metasurfaces: Simultaneous control of spontaneous emission and far-field radiation, Nano Lett. **18**, 6906 (2018).

[8] T. Galfsky, H. N. S. Krishnamoorthy, W. Newman, E. E. Narimanov, Z. Jacob, and V. M. Menon, Active hyperbolic metamaterials: Enhanced spontaneous emission and light extraction, Optica **2**, 62 (2015).

[9] Z. Zhenrong, H. Xiang, and L. Xu, Freeform surface lens for led uniform illumination, Appl. Opt. **48**, 6627 (2009).

[10] E. F. Schubert, *Light-Emitting Diodes* (Cambridge University Press, Cambridge, 2000), 2nd ed., Chap. 5, p. 86.

[11] K. G. Sullivan, O. King, C. Sigg, and D. G. Hall, Directional, enhanced fluorescence from molecules near a periodic surface, Appl. Opt. **33**, 2447 (1994).

[12] W. L. Barnes, Fluorescence near interfaces: The role of photonic mode density, J. Mod. Opt. **45**, 661 (1998).

[13] W. Holland and D. G. Hall, Waveguide mode enhancement of molecular fluorescence, Opt. Lett. **10**, 414 (1985).

[14] A. Vaskin, J. Bohn, K. E. Chong, T. Bucher, M. Zilk, D.-Y. Choi, D. N. Neshev, Y. S. Kivshar, T. Pertsch, and I. Staude, Directional and spectral shaping of light emission with mie-resonant silicon nanoantenna arrays, ACS Photonics **5**, 1359 (2018).

[15] E. Khaidarov, Z. Liu, R. Paniagua-Domínguez, S. T. Ha, V. Valuckas, X. Liang, Y. Akimov, P. Bai, C. E. Png, and H. V. Demir, Control of led emission with functional dielectric metasurfaces, Laser Photonics Rev. **14**, 1900235 (2020).

[16] G. Lozano, G. Grzela, M. A. Verschuuren, M. Ramezani, and J. G. Rivas, Tailor-made directional emission in nanoimprinted plasmonic-based light-emitting devices, Nanoscale **6**, 9223 (2014).

[17] J. J. Wierer Jr, A. David, and M. M. Megens, Iii-nitride photonic-crystal light-emitting diodes with high extraction efficiency, Nat. Photonics **3**, 163 (2009).

[18] L. Langguth, D. Punj, J. Wenger, and A. F. Koenderink, Plasmonic band structure controls single-molecule fluorescence, ACS nano **7**, 8840 (2013).

[19] T. Bucher, A. Vaskin, R. Mupparapu, F. J. Löchner, A. George, K. E. Chong, S. Fasold, C. Neumann, D.-Y. Choi, and F. Eilenberger, Tailoring photoluminescence from mos2 monolayers by mie-resonant metasurfaces, ACS Photonics **6**, 1002 (2019).

[20] S. Bidault, M. Mivelle, and N. Bonod, Dielectric nanoantennas to manipulate solid-state light emission, J. Appl. Phys. **126**, 094104 (2019).

[21] D. Leykam and S. Flach, Perspective: Photonic flatbands, Apl Photonics **3**, 070901 (2018).

[22] S. R. K. Rodriguez, S. Murai, M. A. Verschuuren, and J. G. Rivas, Light-Emitting Waveguide-Plasmon Polaritons, Phys. Rev. Lett. **109**, 166803 (2012).

[23] S. I. Azzam, V. M. Shalaev, A. Boltasseva, and A. V. Kildishev, Formation of Bound States in the Continuum in Hybrid Plasmonic-Photonic Systems, Phys. Rev. Lett. **121**, 253901 (2018).

[24] A. Christ, S. G. Tikhodeev, N. A. Gippius, J. Kuhl, and H. Giessen, Waveguide-Plasmon Polaritons: Strong Coupling of Photonic and Electronic Resonances in a Metallic Photonic Crystal Slab, Phys. Rev. Lett. **91**, 183901 (2003).

[25] D. M. Whittaker and I. S. Culshaw, Scattering-matrix treatment of patterned multilayer photonic structures, Phys. Rev. B **60**, 2610 (1999).

[26] E. Popov and M. Nevière, Maxwell equations in fourier space: fast-converging formulation for diffraction by arbitrary shaped, periodic, anisotropic media, J. Opt. Soc. Am. A **18**, 2886 (2001).

[27] W. L. Barnes, T. W Preist, S. C. Kitson, and J. R. Sambles, Physical origin of photonic energy gaps in the propagation of surface plasmons on gratings, Phys. Rev. B **54**, 6227 (1996).

[28] S.-G. Lee and R. Magnusson, Band flips and bound-state transitions in leaky-mode photonic lattices, Phys. Rev. B **99**, 045304 (2019).

[29] A. F. d. Mota, A. Martins, H. Ottevaere, W. Meulebroeck, E. R. Martins, J. Weiner, F. L. Teixeira, and B.-H. V. Borges, Semi-analytical model for design and analysis of grating-assisted radiation emission of quantum emitters in hyperbolic metamaterials, ACS Photonics **5**, 1951 (2018).